Journal of Modern Optics
2009, 1–6, iFirst

Taylor & Francis
Taylor & Francis Group

Accelerating electrons with lasers and photonic crystals

C. McGuinness[a]*, E. Colby[a] and R.L. Byer[b]

[a]*SLAC National Accelerator Laboratory, 2575 Sand Hill Road MS7, Menlo Park, CA 94025, USA;*
[b]*E.L. Ginzton Laboratory, Stanford University, Stanford, CA 94305, USA*

(*Received 23 March 2009; final version received 7 September 2009*)

We present work done towards the successful fabrication of a four-layer woodpile photonic crystal with a bandgap of 0.876 μm centered at 4.55 μm. The goal of this fabrication was to develop a process flow that will be used to fabricate a 15-layer woodpile structure with a defect used for accelerating electrons. The structure dimensions were designed using simulations to maximize the bandgap, and scaled by the minimum features achievable in the optical lithography process. Infrared spectroscopy measurements were taken of the resulting four-layer structure, demonstrating a clear bandgap region centered at 4.55 μm, with a full-width at half maximum (FWHM) of 2.72 μm. Variations in the actual fabricated structure were measured via SEM images, and the deviations were incorporated into simulations. The center bandgap wavelength predicted in simulations agrees to within 1% of the measured value, and the FWHM agrees to within 15% of the measurement. These results provide validation for the quality of the photonic crystal fabricated.

Keywords: laser acceleration; photonic crystal; woodpile; electrons; lithography; FTIR

1. Introduction

Research in particle accelerators has historically been driven by the application of colliders in particle physics and synchrotrons for radiation generation. Current projects using free electron lasers for X-ray generation, such as LCLS and XFEL, provide further motivation for advancements in accelerator technology. Laser-driven dielectric accelerator structures have recently become of interest due to the potential GeV/m accelerating gradients [1,2], widespread availability of high power lasers, low costs associated with large-scale fabrication of lithographic structures, and attosecond bunch lengths in such accelerating schemes [3–5]. High loss in metals at optical frequencies prompts exploration of alternative means for confinement and manipulation of the electromagnetic (EM) fields used for laser acceleration. Photonic crystals offer an attractive way to confine laser radiation to a defect region, allowing for the manipulation of the EM fields without the use of metallic boundaries. One structure in particular that has been explored in some detail, but only theoretically for particle accelerator applications, is the woodpile structure, shown in Figure 1(*a*). This structure is attractive because it has a fully three-dimensional bandgap, is amenable to common lithographic procedures, and allows for much flexibility in structure refinement and modification of particular features, such as couplers or focusing elements.

The critical parameters for the design of a woodpile accelerator structure have been explored through simulations by Cowan [2]. These simulations provide the framework needed to guide the initial steps of fabrication. Structure parameters are dimensionless in simulations, scaling in proportion to the lattice constant, a, of the structure. The rod width, w, was determined in simulations by maximizing the bandgap. In order to maintain a face-centered cubic (FCC) crystal structure, the layer thickness, h, was held to $\frac{\sqrt{2}}{4}a$. The actual scale of the structure was limited by the minimum features achievable in the lithography process, setting a minimum rod width of 500 nm. These dimensions correspond to a structure with a center bandgap wavelength of 4.88 μm. Ultimately, the structure dimensions will be chosen to correspond to the wavelength that maximizes the damage threshold. In this paper we discuss the process used to fabricate a four-layer test structure, some spectroscopy measurements of the resulting structure, and a comparison of these measurements to simulations. We will begin with a brief discussion of the theoretical gradient achievable with this structure.

2. Gradient

The peak accelerating gradient for a given structure is determined by the peak damage threshold of the

*Corresponding author. Email: cmcg@stanford.edu

ISSN 0950–0340 print/ISSN 1362–3044 online

DOI: 10.1080/09500340903318539
http://www.informaworld.com

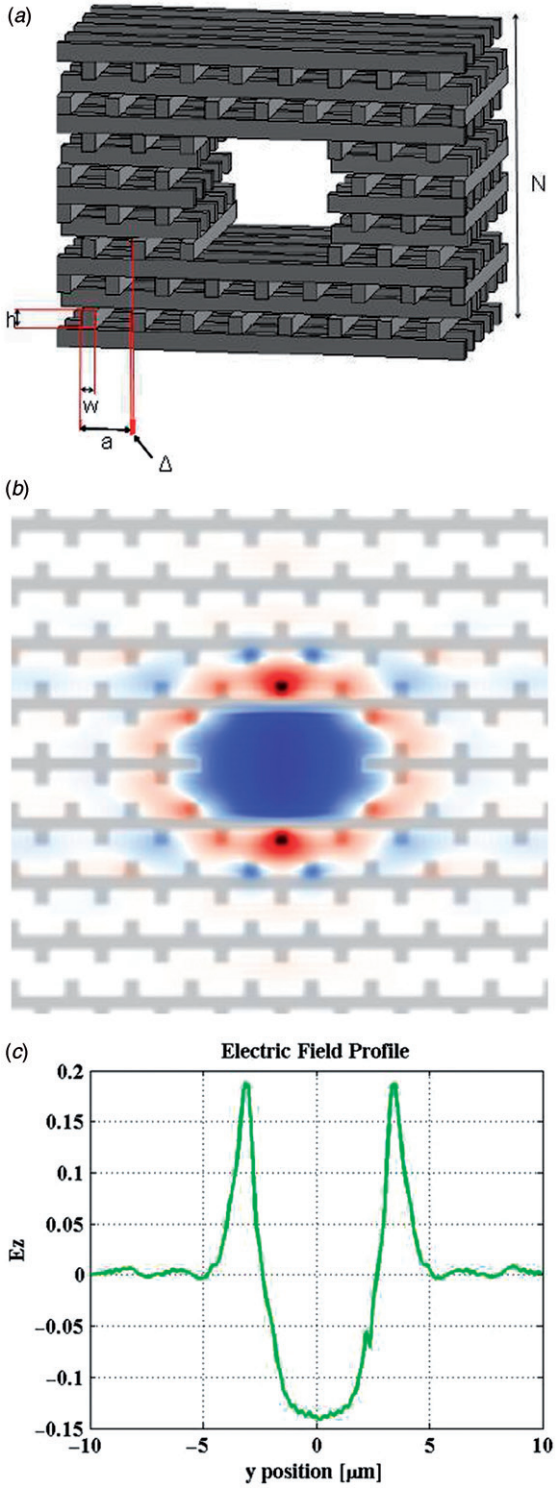

Figure 1. (*a*) A schematic of the woodpile structure design. (*b*) Cross-section of the longitudinal electric field component for the accelerating mode in the woodpile structure. (*c*) The amplitude of the field taken for a vertical slice down the center of the structure used to compare the ratio of the peak electric field in the dielectric to that in the defect. This structure geometry simulated for silicon yields an electric field ratio of 1.44. (The color version of this figure is included in the online version of the journal.)

material and the ratio of the electric field in the material to that in the defect for the particular accelerating mode. The damage threshold of a material, often measured as the damage fluence, depends on the index of refraction of the material, the wavelength, and the pulse width of the applied electric field. Damage fluence for a variety of dielectric materials, at a variety of wavelengths, and for a variety of pulse lengths have been reported previously [68]. For example, a one picosecond long pulse at 4.5 μm has a damage fluence of 6.5 J/cm^2 in calcium fluoride (CaF_2) and 1.5 J/cm^2 in zinc sulfide (ZnS) [6], while a one picosecond long pulse at 1.9 μm has a damage fluence of only 0.29 J/cm^2 in silicon [7]. Using these data as an upper bound for the damage threshold, an upper bound for the accelerating gradient can be determined for a mode in a given structure.

Figure 1(*b*) shows the longitudinal electric field for the accelerating mode, that is a TM_{01}-like mode for a woodpile structure made of silicon. This mode has a phase velocity equal to c, group velocity equal to $0.269c$, minimal dipole and quadrupole field components, and fairly uniform longitudinal electric field amplitude across the defect. Comparing the electric field amplitude along a vertical slice down the center of this profile, shown in Figure 1(*c*), yields a ratio of 1.44 for the peak field in the material to that in the defect. Given the damage fluence and pulse length one can compute the damage threshold:

$$u_{th} = \frac{F_{th}}{2\tau c},$$

where F_{th} is the damage fluence and τ is the pulse length. This corresponds to a maximum electric field sustainable in the material given by:

$$E_{peak} = \sqrt{\frac{2u_{th}}{\epsilon_o}}.$$

Taking the damage fluence to be $0.3\frac{J}{cm^2}$ for a one picosecond long pulse at 1.9 μm in silicon [7], one computes a theoretical accelerating gradient of 337 MV/m for the woodpile structure made of silicon. Other materials, such as calcium fluoride or silicon dioxide, have much higher damage fluences than silicon, by an order of magnitude or more, and could potentially lead to structures with accelerating gradients of several GV/m. However, these materials also have a lower index of refraction, which reduces the size of the photonic bandgap. In silicon dioxide, for example, the bandgap disappears completely for a woodpile geometry. Further investigation into modes supported by these types of structures would be of interest but are not considered here. In this paper, we restrict our discussion to the analysis of a silicon woodpile structure only.

3. Fabrication process

The fabrication process developed for the woodpile structure described here is based upon previous work reported by Lin and Flemming at Sandia National Laboratory [9] and Noda at Kyoto University [10]. Some of the steps were altered to accommodate the tools available at the Stanford Nanofabrication Facility (SNF) in order to achieve the desired structure parameters. The general process involves building the structure layer by layer, using silicon dioxide as a matrix in which silicon features are embedded. When all the layers are complete, a selective etch removes the silicon dioxide, yielding a free-standing structure of silicon and vacuum. Figure 2 shows a visual outline of the process.

The zeroth step in the fabrication is to etch alignment features into the bare silicon wafer. An ASML PAS 5500 i-line stepper interferes two slightly different frequency lasers over the alignment pattern to achieve an alignment accuracy of $3\sigma = 60$ nm. Step one uses low-pressure chemical vapor deposition (LPCVD) of tetraethyl orthosilicate gas (TEOS) to produce a uniform and conformal coating of silicon dioxide. At temperatures greater than 600°C, TEOS breaks down into silicon dioxide, which is deposited on the samples in the deposition chamber, and diethylether, which is collected as waste gas. This step is critical for determining the layer thickness of the final structure, and hence a well controlled and highly uniform deposition is desired. The uniformity between wafers in the chamber and across a given wafer initially varied by 10% and 5%, respectively. By rotating the wafers and inverting their positions within the chamber half way through a given run, the uniformity was improved to 2% between wafers and across a given wafer. The controllability, defined here as the difference between the desired layer thickness and that actually achieved, was 5%.

The second and third steps involve lithographically imaging the desired pattern for the given layer into a coating of resist spun onto the wafers. A 0.7 μm thick layer of Megaposit SPR955-CM i-line resist is coated on the wafer and then exposed with an image of the desired pattern from the mask using the ASML PAS 5500 i-line stepper. This step limits the structure dimensions to minimum features of 450 nm. The rod width, w, is the minimum feature for the structure, and 500 nm was chosen as the target rod width for this four layer structure. Future structures will attempt to resolve 400 nm rod widths. Once the resist is exposed, the wafers are developed in Microposit MF-26A developer and baked at 110°C for 90 seconds.

Step four uses an AMT 8100 hexode plasma etcher to etch the features patterned into the resist into the oxide layer below. Variations in the etch rate across the machine are problematic, due to the potential for under-etching. An under-etched layer will not contact the layer beneath, and during the final selective oxide removal these layers will peel apart. To compensate for this problem an additional 7% was added to the etch time, leading to an overlap between successive layers. Once the etch is complete, the resist is removed in a

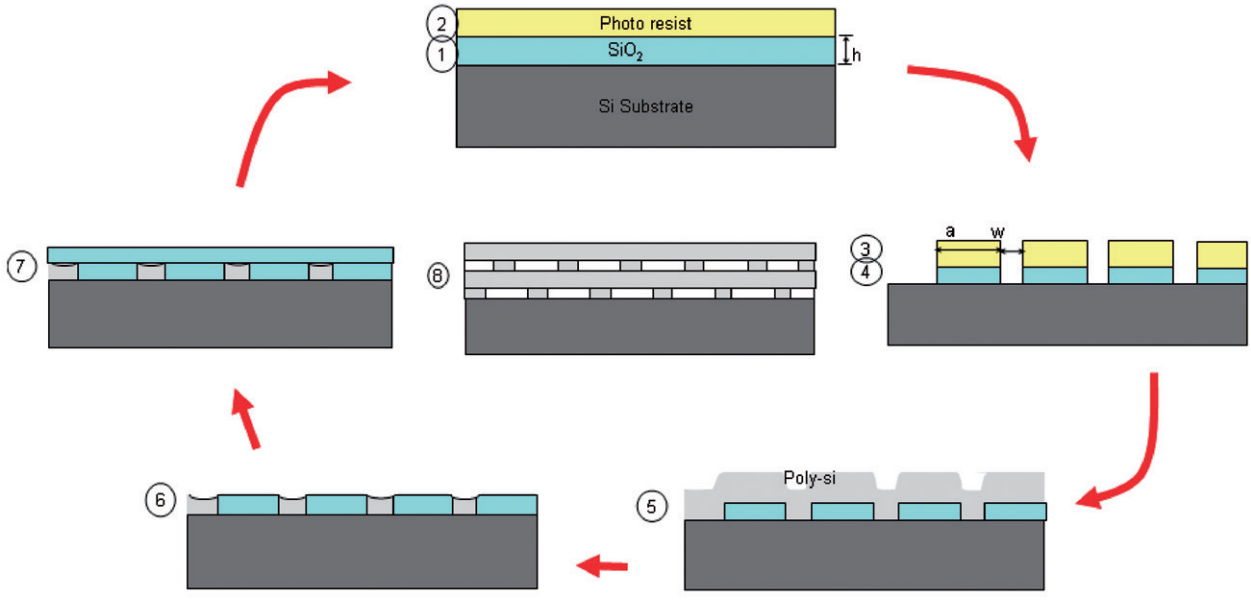

Figure 2. This is a visual outline of the fabrication process. The numbers next to each of the images correspond to the step of the process described in Section 3 of this paper. (The color version of this figure is included in the online version of the journal.)

concentrated solution of sulphuric acid and hydrogen peroxide.

The fifth step involves LPCVD of poly-crystalline silicon at 620°C. This deposition isotropically coats the patterned surface of the silicon dioxide, filling in the etched features with poly-silicon, as demonstrated in the diagram of the process flow in Figure 2.

The sixth step is to chemical-mechanical polish (CMP) the surface of the deposited silicon down to the surface of the oxide. The CMP tool used for this step is equipped with an end-point detector, which measures the friction in the polishing chuck. This allows one to detect a change in friction when the surface of the oxide is reached. The detected change in friction occurs over 20 seconds, which corresponds to a potential polishing depth of 24 nm in oxide or 3.7% of the layer thickness. This over-polish is accounted for during the initial oxide deposition in step one.

Once the wafers are planarized on the CMP tool, the entire process is repeated for the next layer by depositing another layer of oxide and proceeding exactly as done for the first layer. This continues for the desired number of layers. When all the layers are complete, a selective oxide etch is performed using a buffered oxide etch consisting of 34% ammonium fluoride (NH_4F) and 7% hydrofluoric acid (HF) in water. This selectively etches the oxide, leaving the stack of silicon rods free standing surrounded by vacuum or air.

4. Results

A four-layer test structure was successfully fabricated using the process flow described here, and is shown in Figure 3(*a*). A detailed profile image was taken, shown in Figure 3(*b*), which reveals slight variations in the final structure. For example, Figure 3(*b*) shows a slight taper to the rod profiles and slight variations in rod width between successive layers. To characterize the quality of the fabricated photonic crystal and measure the effect of these variations, spectroscopy measurements were taken. These measurements were performed using a Nicolet 6700 Fourier transform infrared spectrometer (FTIR). A temperature-controlled source was used to produce a broad output from 3–25 μm, which was focused onto the sample through a Cassegranian objective with a numerical aperture of 0.58. The reflected light was recollected using the same objective and an interferogram was produced. The Fourier transform of the resulting interferogram yields the reflectivity of the sample as a function of wavelength. Figure 4 shows the reflection spectrum for two of the structures. The measured spectrum is normalized to data taken for an unpatterened region of the wafer,

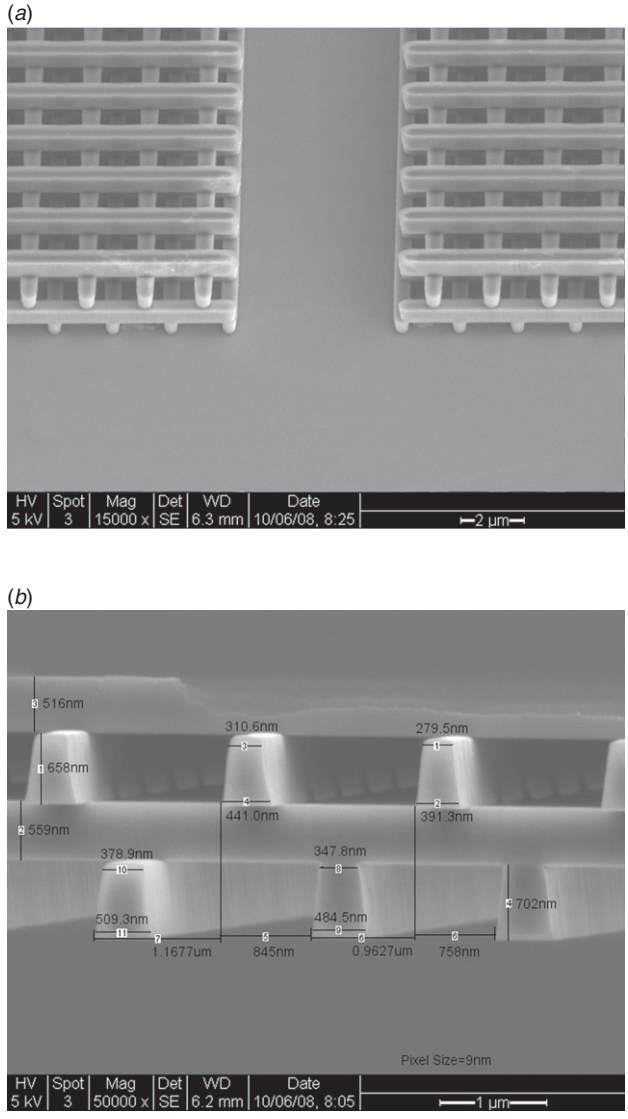

Figure 3. (*a*) SEM image of the successfully fabricated four layer woodpile structure. The gap between the two patterned regions shown serves as a demonstration of the ultimate defect to be fabricated in the 15-layer woodpile structure shown schematiclally in Figure 1(*a*). (*b*) A profile image showing details of the fabricated structure. Slight variations in rod width, layer thickness, and layer-to-layer alignment were measured using this image and incorporated into simulations.

shown by the solid lines, and to a gold mirror, shown by the dotted lines. We observe a clear peak in reflectivity centered at 4.51 μm with a FWHM of 2.62 μm. Note, the reflectivity of the structure exceeds that of gold at 4 μm, which has a reflectivity of 95% at this wavelength.

The measured reflection spectrum was analyzed by comparing it with simulations of the fabricated structure. Simulations were performed using a rigorous coupled-wave analysis (RCWA) code, in which eigenmode solutions for a given 2D plane are computed,

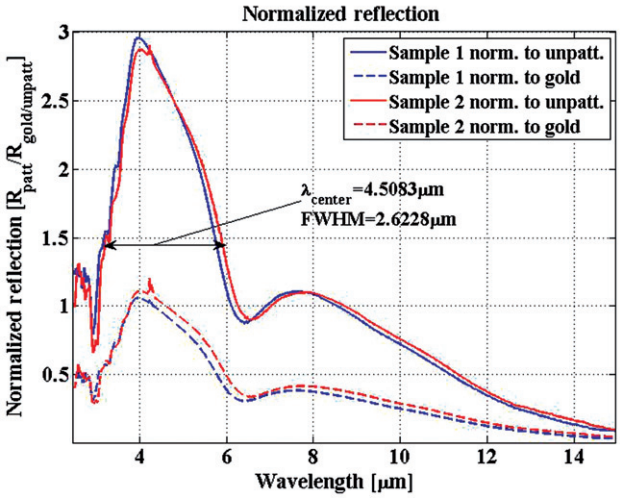

Figure 4. Measured reflection spectrum for two samples of the four layer woodpile structure. The solid line corresponds to data normalized to measurements made on an unpatterened region of the wafer. The dashed line corresponds to data normalized to a gold mirror, with approximately 95% reflectivity across this range of wavelengths. (The color version of this figure is included in the online version of the journal.)

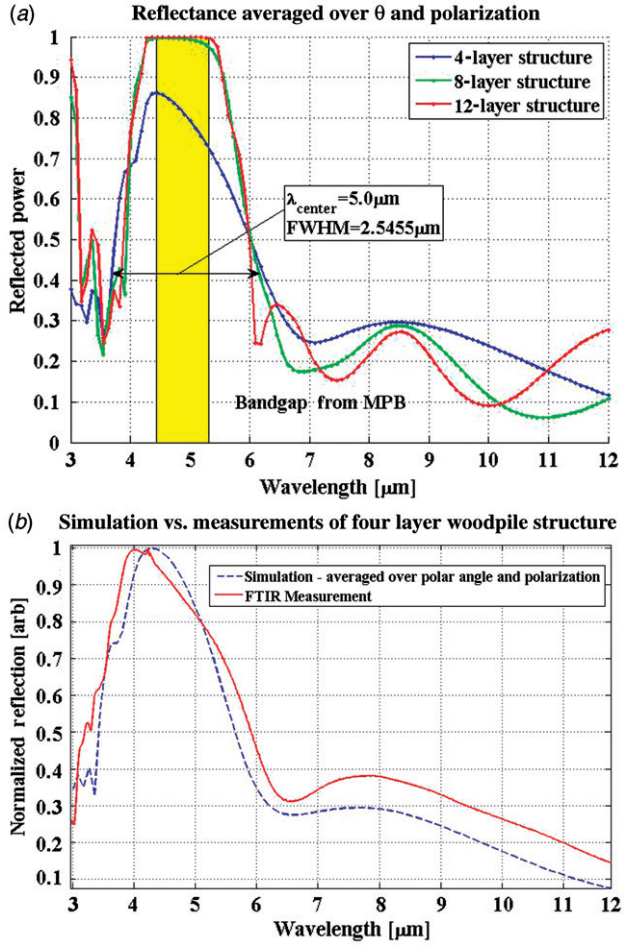

Figure 5. (*a*) Simulated reflection spectrum for a four-, eight-, and 12-layer woodpile structure using the RCWA code. The bandgap region calculated from MPB is overlayed showing good agreement as the number of layers increases, providing validation for the new code. (*b*) Simulation and measurements agree nicely when the fabrication deviation are modeled appropriately in the simulations. The measured center bandgap wavelength is 4.55 μm compared with 4.59 μm for simulations. The FWHM for the measurement was 2.72 μm compared with 2.27 μm for simulations. (The color version of this figure is included in the online version of the journal.)

assuming an infinite plane with a periodically modulated index of refraction. The field solutions for each plane are propagated from layer to layer using the scattering matrix method [11]. This code is uniquely situated to simulate this problem because it does not assume an infinite 3D lattice but rather a series of infinite 2D planes stacked on top of one another. In addition, this code allows one to model a structure with variations between successive layers. The code was benchmarked against MIT's photonic bands (MPB) code by similating an ideal structure with four, eight, and 12 layers. Figure 5(*a*) shows the resulting spectrum from this benchmark comparison, along with the bandgap computed by MPB. As expected, the bandgap becomes more clearly defined with the addition of layers showing good agreement with MPB. Once the code was benchmarked, simulations were performed using the structure dimensions, such as rod width, layer thickness, and layer-to-layer alignment, measured in Figure 3(*b*). To more closely approximate the measurement method, the simulation results were averaged over 10 polar angles and both S and P polarizations. Figure 5(*b*) shows the simulation results, compared to the measured reflection spectrum. Agreement in the center bandgap wavelength, determined by taking the center of the FWHM, is within 1% and the width of the bandgap is within 15%, where the measured bandgap is larger than in the simulation. Qualitative agreement in the features at the shorter and longer wavelength ends of the spectrum can also be seen, though are difficult to compare quantitatively. These results validate the quality of the photonic crystal and the fabrication process.

5. Conclusion

A four-layer woodpile structure was successfully fabricated and initial spectroscopic measurements have been taken. Computational tools were developed to model the finite-layered woodpile structure.

The simulations show good agreement with the spectroscopy measurements taken for the four-layer structure when accounting for fabrication deviations. The fabrication deviations caused the bandgap to shift to lower wavelengths but did not affect the actual width of the bandgap significantly. Future improvements to the process flow will address the tapering of the etch, the alignment between layers, and rod width deviations. A 15-layer structure with a defect channel is currently under fabrication. Optical and electron beam wakefield measurements will be performed on this structure.

Acknowledgments

The author would like to thank the SNF staff for their help with the entire fabrication process, with particular thanks to Mary Tang, Maurice Stevens, Mahnaz Mansourpour, Ed Myers, Nancy Latta, and Uli Thumser. Thanks also to Anthony Serpry for developing the RCWA code used for the simulations and to Jon Schuller for the use of the FTIR used for the spectroscopy measurements. Work supported by Department of Energy contracts DE-AC02-76SF00515 (SLAC) and DE-FG03-97ER41043-II (LEAP).

References

[1] Lin, X.E. *Phys. Rev. STAB* **2001,** *4,* 051301.
[2] Cowan, B.M. *Phys. Rev. STAB* **2008,** *11,* 011301.
[3] Sears, C.M.S.; Colby, E.; England, R.J.; Ischebeck, R.; McGuinness, C.; Nelson, J.; Noble, R.; Siemann, R.H.; Spencer, J.; Walz, D.; Plettner, T.; Byer, R.L. *Phys. Rev. STAB* **2008,** *11,* 101301.
[4] Siemann, R.H. *Phys. Rev. STAB* **2004,** *7,* 061303.
[5] Na, Y.C.N.; Siemann, R.H.; Byer, R.L. *Phys. Rev. STAB* **2005,** *8,* 031301.
[6] Simanovskii, D.M.; Schwettman, H.A.; Lee, H.; Welch, A.J. *Phys. Rev.* **2003,** *91,* 107601.
[7] Cowan, B.M. Photonic Crystal Laser-driven Accelerator Structures. Ph.D. Dissertation, Stanford University, Palo Alto, CA, 2007.
[8] Mero, M.; Liu, J.; Rudolph, W.; Ristau, D.; Starke, K. *Phys. Rev. B* **2005,** *71,* 115109.
[9] Lin, S.Y.; Flemming, J.G.; Hetherington, D.L.; Smith, B.K.; Biswas, R.; Ho, K.M.; Sigalas, M.M.; Zubrzycki, W.; Kurtz, S.R.; Burr, J. *Nature* **1998,** *394,* 251–253.
[10] Noda, S. *J. Lightwave Technol.* **2006,** *24,* 4554–4567.
[11] Tikhodeev, S.G.; Yablonskii, A.L.; Muljarov, E.A.; Gippius, N.A.; Ishihara, T. *Phys. Rev. B* **2002,** *66,* 045102.